Research Article Vol. 34, No. 6 / 23 Mar 2026 / Optics Express 11271
Optics EXPRESS

Freeform maskless nanolithography of silicon via subsurface laser writing

BELIZ DOGUKAYA,[1] RANA ASGARI SABET,[1] AND ONUR TOKEL[1,2,*]

[1]Department of Physics, Bilkent University, Ankara 06800, Turkey
[2]National Nanotechnology Research Center, Bilkent University, Ankara 06800, Turkey
[*]otokel@bilkent.edu.tr

Abstract: Functional nanostructuring of crystalline silicon typically relies on mask-based lithography or laser methods restricted to periodic textures. We report a subsurface-to-surface laser-writing approach that patterns silicon without masks or resists, enabling programmable freeform nanoscale features. Etch-selective seeds are inscribed tens of micrometers beneath the surface, and routine polishing followed by a brief wet etch converts them into deterministic nanoscale surface reliefs. The method affords precise, reproducible geometric control, including curved motifs, and yields linewidths down to 250 nm at 800 nm pitch. In single scans over 3-mm^2 fields, we fabricate high-aspect-ratio nanogratings exhibiting ~25% relative diffraction efficiency at 532 and 633 nm. By leveraging the design freedom of volumetric laser modification, this strategy provides a route to structural color, light-management textures, and silicon metasurfaces for nanophotonics.

1. Introduction

Silicon (Si) is the foundational material of modern electronics, photovoltaics and Si-photonics [1–3]. Conventional fabrication techniques produce diverse functional devices and systems across the wafer surface, broadly referred to as *on-chip*. Recently, an alternative *in-chip* paradigm has emerged [4–6], enabling functionality directly within the wafer volume. In this approach, infrared laser pulses induce structural modifications deep inside the wafer, without affecting the surrounding material. Three-dimensional (3D) microstructures can be inscribed using either nanosecond [4] or ultrafast laser pulses [7,8]. By tailoring the optical and material response of these localized modifications, a wide range of volumetric photonics and microscale applications has been demonstrated, including 3D lenses [9], high-efficiency gratings [10], waveplates [11], holograms [4], microchannels [12], and waveguides [7,13–15]. More recently, subsurface nanostructuring beyond the diffraction limit has been achieved [5] through spatially modulated nondiffractive beams and a bulk seeding effect. This approach enables high-aspect-ratio nanostructures with features as small as 100 nm [5], and functional nanophotonic elements inside the wafer [5]. Comparable advances are also emerging in other transparent solids [16–19], pointing to a general platform for volumetric photonics.

Building on this subsurface control, we extend the in-chip paradigm to surface nanolithography. Established planar nanolithography techniques, such as electron-beam lithography (EBL) [20], focused ion beam milling (FIB) [21] and nanoimprint lithography (NIL) [22] can achieve sub-10 nm resolution, but remain complex and capital-intensive, relying on masks/templates (NIL) and stringent cleanroom environments [20,22,23]. To overcome these limitations, laser-based methods have been explored, including laser-induced periodic structuring (LIPSS) [24,25], laser interference lithography (LIL) [26] and direct laser writing (DLW) [27]. By their very nature, LIPSS and LIL are limited to creating periodic patterns dictated by the symmetry of interfering fields, precluding genuine freeform nanopatterning [28,29]. While semi-circular and curved motifs have been reported in LIPSS, they lack true freeform capability and deterministic

#580993 https://doi.org/10.1364/OE.580993
Journal © 2026 Received 7 Oct 2025; revised 7 Dec 2025; accepted 26 Jan 2026; published 19 Mar 2026

Optics EXPRESS

long-range control [30–34]. DLW, in principle, supports freeform fabrication [35]; however, without reliance on masks, resists or near-field enhancement strategies, its application to Si remains limited, with most advances restricted to linear grooves or arrays [27,36,37].

Here, we introduce a laser-based method for freeform nanolithography with deterministic long-range order (Fig. 1). Our method combines fully ambient tabletop laser writing with minimal post-processing, limited to standard polishing and a brief wet etch. In contrast to conventional nanolithography, it is rapid (completed in under 45 min), mask- and resist-free, and requires no cleanroom infrastructure. The three-step workflow, the laser writing setup, and representative SEM images are illustrated in Figs. 1(a)–1(b). In Step 1, nanostructures are inscribed by three-dimensional (3D) laser writing, where spatially-modulated laser pulses enable rapid, continuous subsurface nanopatterning [5] (see Methods). Step 2 transfers the embedded nanopatterns to the surface via mechanical polishing, while preserving the surface quality comparable to pristine Si. Step 3 applies a brief selective etch to remove the laser-modified regions, thereby revealing the programmed nanopattern over the surface (Fig. 1(b)).

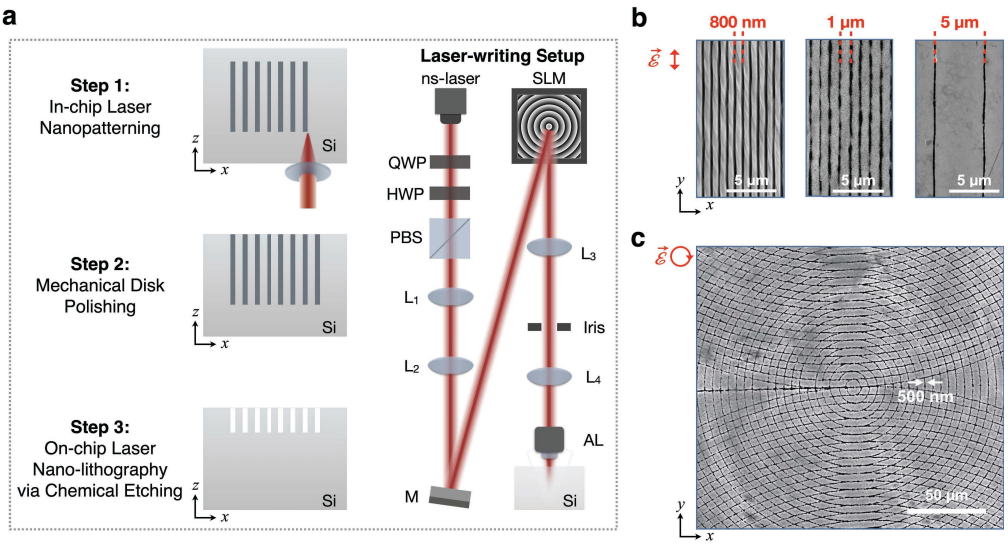

Fig. 1. Overview of freeform laser nanolithography method. **(a)** Schematic of the three-step process and the laser-writing setup: in-chip laser nanopatterning, mechanical polishing, and selective wet etching are used to reveal programmed surface features. A quarter-wave plate (QWP), a half-wave plate (HWP) and a polarizing beam splitter (PBS) are used to adjust the laser power and polarization. Lenses L_1 and L_2 act as a beam expander, and mirror M directs the beam onto the spatial light modulator (SLM). Filtering is performed by a 4-f system with L_3 and L_4 lenses and an iris. Finally, an aspheric lens (AL) focuses the laser inside the sample. The laser propagates along the z-axis. **(b)** Scanning electron microscopy (SEM) images show precise control of periodicity after Step 3, with pitches of 800 nm, 1 μm, and 3 μm. Samples are written at pulse energy $E_p = 7.3$ μJ with linear polarization and etched for 30 s. The feature size is 248 ± 52 nm for 800-nm period sample, 243 ± 80 nm for 1-μm period sample and 236 ± 21 nm for 3-μm period sample. $\vec{\mathcal{E}}$ indicates polarization direction. **(c)** Concentric curved nanostructures illustrating freeform nanopatterning. The sample is written with $E_p = 7.3$ μJ using circular polarization and etched for 30 s, covering an area of 250 μm × 250 μm, with a total fabrication time of ~ 40 min.

The method affords precise and programmable geometry, as each continuous nanoscale line or curve is created with a single scan of the laser. For example, the pitch of periodic patterns can be tuned from several micrometers to nanoscale (as small as 800 nm, Fig. 1(b)), while

Optics EXPRESS

the feature size can be reduced to ~ 250 nm by adjusting laser writing conditions and etching parameters. The method supports complex freeform geometries, including intersecting lines, curved trajectories, and smoothly varying patterns (Fig. 1(c)). This level of control enables virtually arbitrary nanoscale geometries with deterministic long-range order, opening a pathway to advanced nanostructured surfaces for nanoengineering, microsystems, and photonics.

2. Methods

2.1. In-chip laser nanopatterning

In Step 1, buried nanostructures are inscribed in ‹100› p-type, boron-doped Si wafers (1–10 Ω·cm, 1-1.2 mm thick, Siegert) using 10 ns, 1550 nm laser pulses at 150 kHz with 7–10 μJ energy. The details of the experimental setup and the laser system are illustrated in Fig. 1(a). The pulse energy and polarization are controlled with a combination of wave plates and a polarizing beam splitter. The beam is expanded and collimated by lenses, L_1 ($f_1 = 15$ mm) and L_2 ($f_2 = 35$ mm), before being projected onto a Spatial Light Modulator (SLM).

The SLM (Hamamatsu LCOS-SLM, X10468-08, 792×600 pixels, 20 μm pitch) generates a Bessel type modulation [5]. The phase profile, $\phi(r) = \exp(+j2\pi r/r_0)$, is applied where r is the radial coordinate on the device and r_0 is a parameter related to the axicon cone angle, defined as $r_0 = \lambda/\tan\alpha$[5]. The reflected beam is demagnified by a $4f$ system consisting of L_3 ($f_3 = 125$ mm) and L_4 ($f_4 = 100$ mm), to match the aperture of the final aspheric lens ($f = 4.5$ mm).

We adopt the axial convention shown in Fig. 1, with the laser propagating along the z-axis, and both polarization and scanning directions confined to x–y plane. The laser is focused into the sample, by translating Si 40 μm closer to the focusing lens relative to the focal point in air (air-equivalent depth). Beam positioning is controlled using a computer-controlled, high-resolution three-axis translation stage (Aerotech, ANT130XY and ANT95-L-Z). The scan speed is 1 mm/s for all experiments. In SEM images, the laser polarization is indicated on each panel.

The scanning pattern in Step 1 is preserved after Step 3 (Figs. 1(b)–1(c)); for example, each line in Fig. 1(b) corresponds to a single scan along the y-axis. The choice of r_0 parameter and pulse energy, E_p, dictate the resolution [5]. Beam characterization and calibration experiments identify $r_0 = 6$ as optimal (see Supplement 1, Fig. S1). For $r_0 = 6$, the empirical energy threshold for modification is $E_p = 7.3$ μJ, yielding subsurface features of 212 nm ± 46 nm (mean ± std.). Further improvements in resolution may be possible with higher-resolution SLMs.

2.2. Mechanical thinning and surface polishing

A precision polishing system (MultiPrep 10-1000-230, Allied High-Tech Products, Inc.) is used in Step 2 to thin each sample by 150–160 μm. Mechanical polishing proceeds sequentially with diamond lapping films (Allied, 8″ adhesive-backed discs) of 15 μm, 9 μm, 6 μm, 3 μm, 1 μm, 0.5 μm, 0.25 μm, and 0.1 μm grit sizes, from coarsest to finest. A continuous flow of water is maintained throughout to remove debris. Stage parameters and polishing depths are listed in Supplement 1, Table S1. Polishing depth is verified with a calibrated digital indicator (Mitutoyo 543-472B). Surface quality before and after polishing is evaluated with a confocal laser scanning microscope (Keyence VK-X100) equipped with a 100× objective, providing depth precision of 5 nm and lateral sampling of 10 nm [38]. Representative surface images and roughness values are shown in Supplement 1, Fig. S2 and Table S2, respectively. Morphology of subsurface structures after polishing to 150–160 μm depth is illustrated in Fig. S3.

2.3. Selective wet etching of laser-modified regions

In Step 3, a hydrofluoric acid (HF)-based etchant is used to selectively remove the laser-modified regions and reveal the surface nanostructures. The etchant consists of copper (II) nitrate trihydrate ($Cu(NO_3)_2{\cdot}3H_2O$, 3 g), hydrofluoric acid (HF, 36 mL, 40%), nitric acid (HNO_3, 25 mL, 65%),

Optics EXPRESS

and acetic acid (CH_3COOH, 24 mL, 100%) [5,12,39]. Etching is carried out in a static bath at room temperature for 20–40 s. After etching, samples are rinsed with DI water and dried under a nitrogen stream. HF (40%) and $Cu(NO_3)_2$ are obtained from Merck, while HNO_3 (65%) and CH_3COOH (100%) are obtained from Sigma-Aldrich. The role of each component in this etchant has been provided and analyzed in Refs. [4,39].

3. Results

3.1. Polarization- and pulse-energy-controlled nanolithography

We find that the feature size, ξ, obtained after Step 3 is governed primarily by laser polarization and pulse energy, E_p. Figure 2(a) shows the dependence of ξ on pulse energy, while we vary E_p from 7.3 to 10 µJ, using a Bessel beam with $r_0 = 6$, for two scan directions; parallel ($\theta = 0^o$) and orthogonal ($\theta = 90^o$) to the laser polarization. The corresponding in-chip structures after Step 1 are given in Supplement 1, Fig. S4. A clear polarization anisotropy emerges after Step 3. When the scan direction aligns with the laser polarization, $\theta = 0^o$, all energies yield nanoscale features (Fig. 2(a)). In contrast, for $\theta = 90^o$, the features are predominantly microscale for $E_p > 7.3$ µJ, and remain submicron close to the empirical modification threshold of $E_p = 7.3$ µJ.

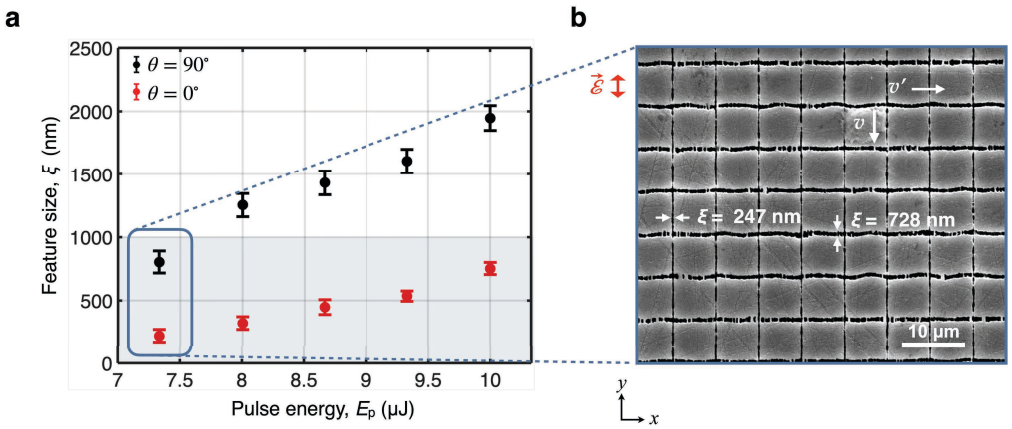

Fig. 2. Polarization and pulse energy dependence of feature size. **(a)** Post-etch feature size versus pulse energy, E_p, for two scan directions relative to linear polarization, parallel ($\theta = 0°$, red) and perpendicular ($\theta = 90°$, black). Nanoscale features are obtained across the full energy range for $\theta = 0°$. All data are acquired with a Bessel beam of $r_0 = 6$ and etched for 30 s. The shaded region denotes the submicron regime. **(b)** SEM of a nanoscale mesh pattern fabricated at $E_p = 7.3$ µJ with $r_0 = 6$ and etched for 30 s. The feature size is 247 ± 57 nm for structures at $\theta = 0°$ and 728 ± 61 nm for structures at for $\theta = 90°$. $\vec{\mathcal{E}}$ indicates the polarization direction; $\vec{v}$ and $\vec{v}'$ vectors mark scan directions.

A representative SEM image of a mesh pattern is shown in Fig. 2(b) for $E_p = 7.3$ µJ, highlighting the capability to fabricate intersecting, continuous features with the method. We find $\xi = 728$ nm for $\theta = 90^o$ and $\xi = 247$ nm for $\theta = 0^o$. The anisotropy is consistent with prior reports of subsurface nanostructuring in Si, where near-field enhancement induces anisotropic writing [5].

The polarization response is examined by creating concentric nanoscale rings with linearly polarized laser (Fig. 3). We scan 50 circles of varying radius R, using y-polarized Bessel beams of $r_0 = 6$ and $E_p = 7.3$ µJ. To our knowledge this is the first maskless, resist-free realization of curved laser nanolithography on Si (Fig. 3(a)). Notably, each nano-ring is produced by a single continuous laser scan, highlighting the ability to create programmable nanopatterns.

Optics EXPRESS

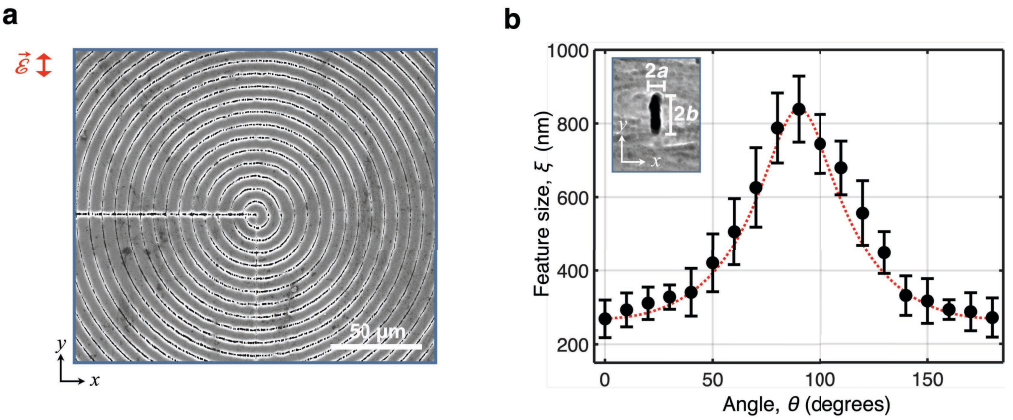

Fig. 3. Feature size variation with polarization alignment. **(a)** Concentric circular nanostructures written with y-polarized, $E_p = 7.3$ µJ pulses. SEM image after Step 3 with 30 s etch. $\vec{\mathcal{E}}$ indicates the polarization direction. **(b)** Feature size ξ as a function of θ measured for radii $R = 14$ µm to $R = 91$ µm with 12 data points per angle. Red dashed curve represents the analytical model. *Inset*: SEM of a single subsurface track written with y-polarized laser and scanned along z, showing an elliptical cross-section elongated along the polarization direction, with semi-axes a and b.

We evaluate the feature size in relation to its polarization alignment. We first define the angle between the scan velocity $\vec{v}$ and $+y$ axis as θ. This also corresponds to the polar coordinate of a point on the circle (Supplement 1, Fig. S5). Then, we extract $\xi(\theta)$ from the SEM analysis and plot in Fig. 3(b). We observe an anisotropic behavior down to $\xi(\theta = 0) = 270$ nm. We shed light on this by developing a simple analytical model (Supplement 1, Fig. S5). We first note that a single subsurface track written along the z axis has an elliptical cross-section in the x-y plane, elongated along the polarization (inset, Fig. 3(b)) [5]. Approximating a circular scan as a tiling of identical, polarization-aligned ellipses with semi-axes a (along x) and b (along y) placed on a circle of radius R, the feature size at the angle θ corresponds to the thickness along the radial direction (Supplement 1, Fig. S5). In the limit of $a, b \ll R$, we find $\xi(\theta) = 2ab / \sqrt{b^2\cos^2\theta + a^2\sin^2\theta}$ (Supplement 1, Fig. S5). Identifying a, b parameters from experiments, we plot the equation in Fig. 3(b), which compares well with experimental results.

We find $\xi = 455 \pm 197$ nm ($n = 228$) for the entire set of rings in Fig. 3(a), which has a significant spread (Fig. 3(b)). The analytical model suggests uniform fabrication for $a = b$, indicating that circular polarization could be used to write uniform, large-area, freeform curves. We demonstrate such motifs using single-pass curved laser scans (Fig. 1(c)). In this case, features exhibit high regularity, $\xi = 519 \pm 74$ nm ($n = 27$). Thus, circular polarization significantly improves the uniformity in curved nanolithography. Taken together, these results establish the polarization state and pulse energy as control parameters for feature size, motivating the use of $\theta = 0^o$ in experiments with linear polarization and circular polarization in curved lithography.

3.2. *Effect of etch duration on nanolithography*

Although the current etch recipe has been reported for microfabrication [12], its behavior at the nanoscale has not been reported. We probe this regime by varying the etch time and tracking the feature size, ξ, and depth, h. Due to high-aspect ratios (h/ξ), Atomic Force Microscopy is unsuitable for depth metrology. The etch depth is quantified by dicing and cross-sectional SEM analysis (Fig. 4(a)). Time dependence of ξ and h for nominally identical structures is shown in Fig. 4(b) and Fig. 4(c), respectively. Our data reveal coupled, nonlinear increase over

Optics EXPRESS

time, with a plateau at 20 - 40 s. To balance precision and reproducibility, we select 30 s as the process set point. Joint analysis of ξ and h yields aspect ratios of ~8–16. Within the submicron regime the highest aspect ratio is 12.6. The influence of pitch on etch rate is further explored in Supplement 1, Fig. S6, enabling high-resolution fabrication ξ ~250 nm, with aspect ratios from 2.7 to 7.1.

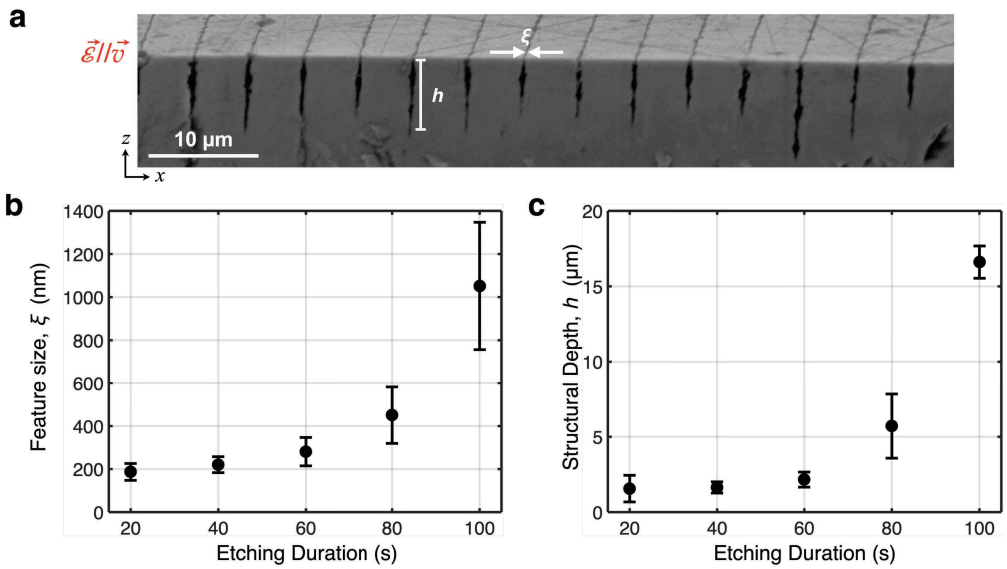

Fig. 4. Feature size and depth variation as a function of etch time. **(a)** Representative cross-sectional SEM image of an array after 80 s etch. The top and cross-sectional planes of the sample are visible, marking ξ and h. **(b)** Feature size, ξ, as a function of etch time. Bessel beams with $r_0 = 6$, $E_p = 7.3$ μJ are used with a scan period of 5 μm. **(c)** Depth, h, as a function of time from the same samples in (b). A stable region is observed for 20–40 s for (b) and (c).

Such high-aspect-ratio fabrication enables functional nanostructuring and provides a basis for engineered spectral and polarization responses. For comparison, LIPSS on Si typically exhibit modulation depths of ~100 nm [40,41], and recent studies report aspect-ratios up to ~8 while remaining submicron in depth [42–44]. By contrast, our structures achieve aspect ratios >10 with depths up to 6 μm while maintaining submicron lateral dimensions.

3.3. *Laser-lithography of visible range gratings*

As a demonstration of the method's capability, we fabricate high-aspect-ratio nanogratings with a feature size of $\xi = 250$ nm and a period $\Lambda = 800$ nm, with depth characterization provided in Supplement 1, Fig. S6. Representative top-view SEM image is shown in Fig. 5(a), together with digital photographs at different viewing angles. Optical performance is assessed by measuring the reflected power (Thorlabs S142C) under illumination with 532 nm (Monocrom DPGL-500L2) and 633 nm (Monocrom LU-63350-100FC) laser sources.

The diffraction efficiency is defined as the ratio of power in diffracted orders to the total reflected power from the grating, $\eta = (I_1 + I_{-1})/I_{\text{reflected}}$ [45]. Measured efficiencies are shown in Figs. 5(b) and 5(c) for 532 nm and 633 nm illumination, respectively. The relative efficiency exceeds 24% at low incidence angles. These results are compared with finite-difference time-domain (FDTD) simulations. In the simulations, the mean grating depth (680 nm ± 65 nm), extracted from SEM

Optics EXPRESS

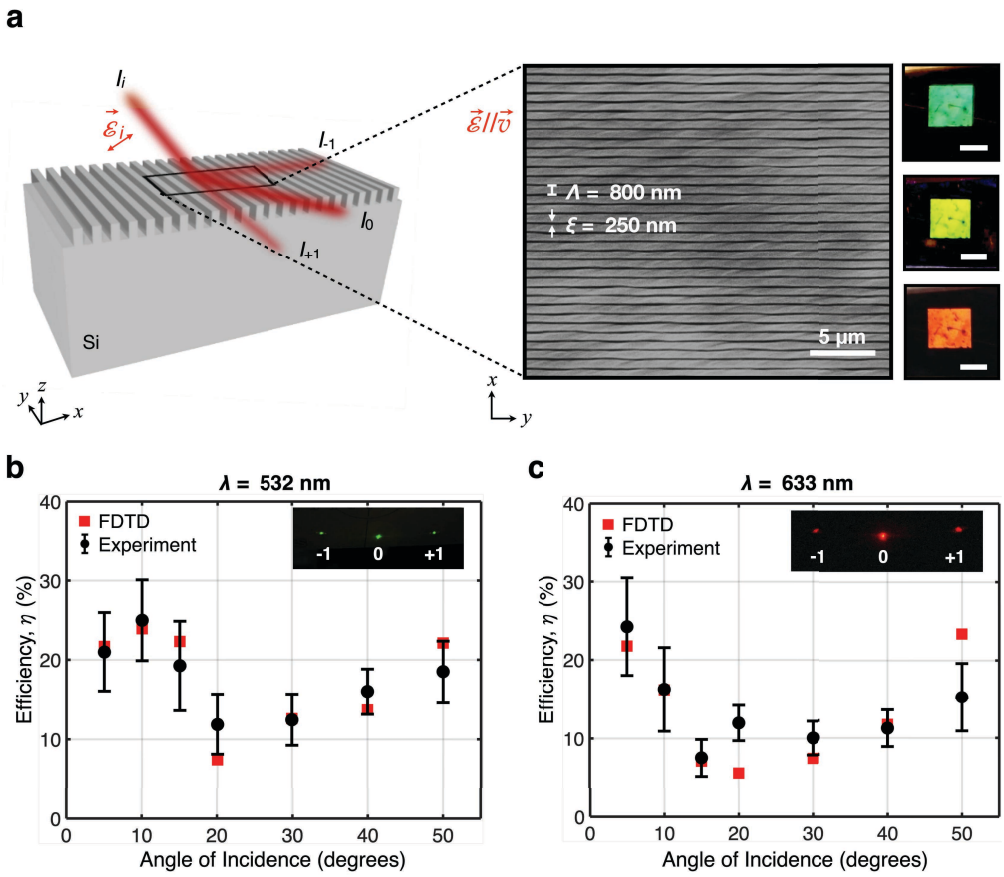

Fig. 5. Optical characterization of nanogratings. **(a)** Schematic of the measurement geometry and SEM of a representative grating with $\xi = 250$ nm and $\Lambda = 800$ nm. The incident beam I_i with polarization direction shown with $\vec{\mathcal{E}}_i$, generates the 0^{th} order reflection I_0, and the ±1st diffraction orders, I_{+1} and I_{-1}. Gratings are fabricated using a Bessel beam of $r_0 = 6$ and $E_p = 7.3$ μJ and etched for 30 s. Inset images: Digital photographs of the fabricated grating at various angles with white light illumination. Structural colors correspond to the grating, while black areas correspond to unprocessed Si. Scalebars: 1 mm. **(b)** Measured and simulated efficiency, η, at $\lambda = 532$ nm as a function of incidence angle. **(c)** Measured and simulated efficiency at $\lambda = 633$ nm. Insets in (b, c) show corresponding diffraction spots.

Optics EXPRESS

cross-sections, is used as an input together with additional parameters summarized in Table 1 to match experimental conditions.

Table 1. FDTD Simulation Parameters

Property	Symbol	Value
Characterization Wavelength	λ	532 nm and 633 nm
Refractive Index at λ	n	4.15 and 3.88
Period	Λ	800 nm
Feature Size	ξ	250 nm
Structural Depth	h	680 nm
Gaussian Depth Error	Δh	± 65 nm

The FDTD simulations reproduce both the angular dependence and the magnitude of η, remaining largely within experimental error bars (Fig. 5). This close agreement validates the approach, demonstrating functional Si nanopatterning with sub-micron periods.

4. Conclusion

We demonstrate a maskless, resist-free, freeform nanolithography route for silicon that translates subsurface writing into deterministic surface reliefs using only routine polishing and a brief selective etch, yielding functional nanostructures. The technique affords deterministic, long-range and programmable control of geometry with linewidths down to $\xi = 250$ nm at $\Lambda = 800$ nm, set by pulse energy, polarization state and scan path. Etch duration serves as an additional knob for depth control, with stable process windows mapped that yield reproducible submicron features with aspect ratios up to 12.6. Crucially, the method supports freeform layouts, including smoothly curved nanoscale patterns produced in a single pass.

Optical performance is confirmed with 800-nm-period reflection gratings operating in the visible regime, delivering ~25% relative first-order diffraction efficiency at 532 and 633 nm, in close agreement with FDTD simulations. Taken together, these results establish subsurface-to-surface laser writing as a robust, mask- and resist-free alternative to conventional lithography and surface laser texturing, opening a practical route to structural color, light-management textures, silicon metasurfaces for integrated and nonlinear photonics, sensing, optofluidics, and nanoelectromechanical systems (NEMS) [46–49].

Funding. Scientific and Technological Research Council of Turkey (1001 Project: 123M873, 2210-A MSc Scholarship).

Disclosures. B.D., R.A.S., and O.T. are inventors on patent application (TR2025/006,747) assigned to Bilkent University based on the work presented here. R.A.S., and O.T. are also inventors on related applications TR2022/007,784 and US17/840,023.

Data availability. Data underlying the results presented in this paper are available within the paper and supporting information.

Supplemental document. See Supplement 1 for supporting content.

References

1. D. G. Baranov, D. A. Zuev, S. I. Lepeshov, *et al.*, "All-dielectric nanophotonics: the quest for better materials and fabrication techniques," Optica **4**(7), 814–825 (2017).
2. X. Chen, M. M. Milosevic, S. Stanković, *et al.*, "The emergence of silicon photonics as a flexible technology platform," Proc. IEEE **106**(12), 2101–2116 (2018).
3. S. Shekhar, W. Bogaerts, L. Chrostowski, *et al.*, "Roadmapping the next generation of silicon photonics," Nat. Commun. **15**(1), 751 (2024).
4. O. Tokel, A. Turnalı, G. Makey, *et al.*, "In-chip microstructures and photonic devices fabricated by nonlinear laser lithography deep inside silicon," Nat. Photonics **11**(10), 639–645 (2017).

Optics EXPRESS

5. R. Asgari Sabet, A. Ishraq, A. Saltik, *et al.*, "Laser nanofabrication inside silicon with spatial beam modulation and anisotropic seeding," Nat. Commun. **15**(1), 5786 (2024).
6. A. Wang, A. Das, V. Y. Fedorov, *et al.*, "In-chip critical plasma seeds for laser writing of reconfigurable silicon photonics systems," Nat. Commun. **16**(1), 6733 (2025).
7. I. Pavlov, O. Tokel, S. Pavlova, *et al.*, "Femtosecond laser written waveguides deep inside silicon," Opt. Lett. **42**(15), 3028–3031 (2017).
8. M. Chanal, V. Y. Fedorov, M. Chambonneau, *et al.*, "Crossing the threshold of ultrafast laser writing in bulk silicon," Nat. Commun. **8**(1), 773 (2017).
9. A. Turnali, O. Tokel, I. Pavlov, *et al.*, "Direct laser writing of volume Fresnel zone plates in silicon," in *2015 European Conference on Lasers and Electro-Optics - European Quantum Electronics Conference* (2015), paper CM_4_5.
10. M. Bütün, S. Saylan, R. Asgari Sabet, *et al.*, "High-efficiency multilevel volume diffraction gratings inside silicon," ACS Materials Au. **3**(6), 727–733 (2023).
11. A. Saltik and O. Tokel, "Laser-written wave plates inside the silicon enabled by stress-induced birefringence," Opt. Lett. **49**(1), 49–52 (2024).
12. M. A. Tauseef, R. A. Sabet, and O. Tokel, "Laser lithography of monolithically-integrated multi-level microchannels in silicon," Adv. Mater. Technol. **9**(9), 2301617 (2024).
13. M. Chambonneau, Q. Li, M. Chanal, *et al.*, "Writing waveguides inside monolithic crystalline silicon with nanosecond laser pulses," Opt. Lett. **41**(21), 4875–4878 (2016).
14. G. Matthäus, H. Kämmer, K. A. Lammers, *et al.*, "Inscription of silicon waveguides using picosecond pulses," Opt. Express **26**(18), 24089–24097 (2018).
15. X. Wang, X. Yu, M. J. Berg, *et al.*, "Curved waveguides in silicon written by a shaped laser beam," Opt. Express **29**(10), 14201–14207 (2021).
16. Z. Z. Li, H. Fan, L. Wang, *et al.*, "Super-stealth dicing of transparent solids with nanometric precision," Nat. Photonics **18**(8), 799–808 (2024).
17. K. Xu, M. Zheng, L. Huang, *et al.*, "All-glass nanohole metalens by non-diffracting laser lithography," Laser Photonics Rev. **19**(14), 2402006 (2025).
18. S. Datta, R. Clady, D. Grojo, *et al.*, "Scalable nanophotonic structures inside silica glass laser-machined by intense shaped beams," Laser Photonics Rev. **18**(9), 2301365 (2024).
19. E. Gribaudo, M. Deckart, P. Vlugter, *et al.*, "Sub-wavelength femtosecond laser based nanostructuring of complex patterns in the bulk of fused silica," Opt. Express **33**(5), 11529–11540 (2025).
20. C. Zhu, H. Ekinci, A. Pan, *et al.*, "Electron beam lithography on nonplanar and irregular surfaces," Microsyst. Nanoeng. **10**(1), 52 (2024).
21. M. V. Gorkunov, O. Y. Rogov, A. V. Kondratov, *et al.*, "Chiral visible light metasurface patterned in monocrystalline silicon by focused ion beam," Sci. Rep. **8**(1), 11623 (2018).
22. M. Zhang, H. Dai, Y. Shang, *et al.*, "Maskless nanostructure photolithography by ultrahigh-order modes of a symmetrical metal-cladding waveguide," Opt. Lett. **47**(1), 62–65 (2022).
23. B. Wen, J. Yang, C. Hu, *et al.*, "Top-down fabrication of ordered nanophotonic structures for biomedical applications," Adv. Mater. Interfaces **11**(5), 2300856 (2024).
24. J. Bonse and J. Krüger, "Pulse number dependence of laser-induced periodic surface structures for femtosecond laser irradiation of silicon," J. Appl. Phys. **108**(3), 034903 (2010).
25. L. Shi, J. Yan, S. Zhang, *et al.*, "Burst laser-driven plasmonic photochemical nanolithography of silicon with active structural modulation," Ultrafast Sci. **5**, 0084 (2025).
26. S. Y. Chou, C. Keimel, and J. Gu, "Ultrafast and direct imprint of nanostructures in silicon," Nature **417**(6891), 835–837 (2002).
27. I. Sakellari, S. Droulias, A. Lemonis, *et al.*, "Femtosecond-laser-induced all-silicon dielectric metasurfaces assisted by wet chemical etching," Ultrafast Sci. **3**, 0019 (2023).
28. S. Lee, K. Jo, H. Keum, *et al.*, "Nanowall formation by maskless wet-etching on a femtosecond laser irradiated silicon surface," Appl. Surf. Sci. **437**, 190–194 (2018).
29. T. Tavera, N. Pérez, A. Rodríguez, *et al.*, "Periodic patterning of silicon by direct nanosecond laser interference ablation," Appl. Surf. Sci. **258**(3), 1175–1180 (2011).
30. W. Liu, J. Hu, L. Jiang, *et al.*, "Formation of laser-induced periodic surface nanometric concentric ring structures on silicon surfaces through single-spot irradiation with orthogonally polarized femtosecond laser double-pulse sequences," Nanophotonics **10**(4), 1273–1283 (2021).
31. Z. Li, S. Bai, H. Chen, *et al.*, "Mechanism study of femtosecond laser-induced periodic surface structures on single-crystal silicon: Insights from two-temperature model and self-organization," J. Laser Appl. **37**(3), 32004 (2025).
32. C. Xiao, T. Wang, X. Wang, *et al.*, "Curved periodic ripples fabricated by double time-delayed femtosecond laser beams on the silicon surface," Opt. Express **29**(10), 14326–14335 (2021).
33. W. Han, F. Liu, Y. Yuan, *et al.*, "Femtosecond laser induced concentric semi-circular periodic surface structures on silicon based on the quasi-plasmonic annular nanostructure," Nanotechnology **29**(30), 305301 (2018).
34. W. Liu, L. Jiang, W. Han, *et al.*, "Manipulation of LIPSS orientation on silicon surfaces using orthogonally polarized femtosecond laser double-pulse trains," Opt. Express **27**(7), 9782–9793 (2019).

Optics EXPRESS

35. Y. Li and M. Hong, "Parallel laser micro/nano-processing for functional device fabrication," Laser Photonics Rev. **14**(3), 1900062 (2020).
36. T. H. R. Crawford, A. Borowiec, and H. K. Haugen, "Femtosecond laser micromachining of grooves in silicon with 800 nm pulses," Appl. Phys. A **80**(8), 1717–1724 (2005).
37. L. T. Tseng, P. Karadan, D. Kazazis, *et al.*, "Resistless EUV lithography: Photon-induced oxide patterning on silicon," Sci. Adv. **9**(16), eadf5997 (2023).
38. W. Cheng, H. Cheng, Y. Feng, *et al.*, "Target-surface multiplexed quantitative dynamic phase microscopic imaging based on the transport-of-intensity equation," Appl. Opt. **62**(26), 6974–6984 (2023).
39. M. Zolfaghari Borra, B. Radfar, H. Nasser, *et al.*, "Development of a selective wet-chemical etchant for precise 3D sculpting of silicon enabled by infrared non-linear laser modification," Opt. Laser Technol. **176**, 111022 (2024).
40. J. Bonse and S. Gräf, "Ten open questions about laser-induced periodic surface structures," Nanomaterials **11**(12), 3326 (2021).
41. E. Granados, M. Martinez-Calderon, B. Groussin, *et al.*, "Highly uniform silicon nanopatterning with deep-ultraviolet femtosecond pulses," Nanophotonics **13**(22), 4079–4089 (2024).
42. K. Bronnikov, A. Dostovalov, V. Terentyev, *et al.*, "Uniform subwavelength high-aspect ratio nanogratings on metal-protected bulk silicon produced by laser-induced periodic surface structuring," Appl. Phys. Lett. **119**(21), 211106 (2021).
43. J. Huang, L. Jiang, X. Li, *et al.*, "Cylindrically focused nonablative femtosecond laser processing of long-range uniform periodic surface structures with tunable diffraction efficiency," Adv. Opt. Mater. **7**(20), 1900706 (2019).
44. H. Vaghasiya and P. T. Miclea, "Laser-induced nano-functional surfaces for enhanced SERS performance," Adv. Mater. Interfaces **12**(14), e00366 (2025).
45. J. Eduardo Ribeiro, H. Lopes, and J. Paulo Carmo, "Characterization of coating processes in Moiré Diffraction Gratings for strain measurements," Opt Laser Technol. **47**, 159–165 (2013).
46. J. E. Fröch, L. Huang, Z. Zhou, *et al.*, "Full color visible imaging with crystalline silicon meta-optics," Light: Sci. Appl. **14**(1), 217 (2025).
47. Y. Zhong, D. Park, S. Xiao, *et al.*, "Wet etching of silicon in planar nanochannels," Langmuir **40**(18), 9501–9508 (2024).
48. J. J. Cadusch, J. Meng, D. Wen, *et al.*, "Compact, lightweight, and filter-free: an all-Si microspectrometer chip for visible light spectroscopy," ACS Photonics **9**(2), 474–481 (2022).
49. R. Meyer, M. Jacquot, R. Giust, *et al.*, "Single-shot ultrafast laser processing of high-aspect-ratio nanochannels using elliptical Bessel beams," Opt. Lett. **42**(21), 4307–4310 (2017).